Nano-to-Micro porous Networks via Inkjet Printing of ZnO Nanoparticles/Graphene hybrid for Ultraviolet Photodetectors

Hanleem Lee[a], William Harden-Chaters[a], Soo Deok Han[a,*], Shijie Zhan[a], Benxuan Li[a], Sang Yun Bang[a], Hyung Woo Choi[a], Sanghyo Lee[a], Bo Hou[a,b*], Luigi G. Occhipinti[a], Jong Min Kim[a]

[a] Department of Engineering, University of Cambridge, 9 JJ Thomson Avenue, Cambridge CB3 0FA, UK

[b] School of Physics and Astronomy, Cardiff University, The Parade, Cardiff, CF24 3AA, UK

*Corresponding Authors: E-mail: sh977@cam.ac.uk (S.D.H.), HouB6@cardiff.ac.uk (B.H.) Tel: +44 (0)1223 748318.

ABSTRACT: Inkjet-printed photodetectors have gained enormous attention over the last decade. However, device performance is limited without post-processing, such as annealing and UV exposure. In addition, it is difficult to manipulate the surface morphology of the printed film using an inkjet printer due to the limited options of low viscosity ink solutions. Here, we employ a concept involving the control of the inkjet-printed film morphology via modulation of co-solvent

vapor pressure and surface tension for the creation of a high-performance ZnO-based photodetector on a flexible substrate. The solvent boiling point across different co-solvent systems is found to affect the film morphology, which results in not only distinct photo-response time but also photo-detectivity. ZnO-based photodetectors were printed using different solvents which display a fast photo-response in low-boiling point solvents due to the low carbon residue and larger photo-detectivity in high-boiling point solvent systems due to the porous structure. The porous structure is obtained using both gas-liquid surface tension differences and solid-liquid surface differences, and the size of porosity is modulated from nano-size to micro-size depending on the ratio between two solvents or two nanomaterials. Moreover, the conductive nature of graphene enhances the transport behavior of the photocarrier, which enables a high-performance photodetector with high photo-responsivity ($7.5*10^2 \, AW^{-1}$) and fast photo-response (0.18 s) to be achieved without the use of high-boiling point solvents.

INTRODUCTION

Recently, printed electronics have considerable interest as a possible candidate to develop large-area electronic systems and flexible electronics at a low cost.[1] Among many other printing techniques, inkjet printing has been considered as a great candidate for the next generation printing method due to several advantages such as its versatility on a wide range of possible substrates, low-temperature processing (20 °C), high processing speeds, mask-less fabrication with a high resolution (~50 μm), manufacturing scalability and low material losses (< 1 mL).[2] Beyond the resistor type film fabrication using conducting materials (e.g., Ag, graphene, and carbon nanotube), technical improvement and in-depth study on this method over the last decade have made it possible to deposit functional ink such as the organic semiconductor,[3] light-emissive polymers,[4] and metal oxide nanoparticles,[5] which are necessary to realise fully printed electronics,

and a wide variety of electronics, such as: a solar cell,[6] light-emitting diode,[7] thin-film transistor,[8] sensor,[9] memory devices[10], which have all been successfully presented up till now. Among them, an inkjet-printed photodetector (PD) is expected to be an essential component for consumable IoTs within optical communication for flexible devices, imaging, light sensing, and hazard detection in the military and medical fields.[11]

The physical and electrical property of films produced by inkjet printing is strongly influenced by the ink formula, including the rheological parameters. Improper ink formula can cause various issues such as the coffee-ring effect, short term ink reliability, and improper drop pinning on the substrate. Previous studies demonstrate the fascinating controllability of organic and polymer functional ink.[12] Several full inkjet printed organic PD have been described and have displayed a similar level of device performance with the devices made using spin coating methods. For example, a fully printed PD with Ag / P3HT: PC61BM/ PEDOT: PSS in a vertical configuration showed good detectivity around $1.5 \times 10^{12} \mathrm{cm} \cdot \mathrm{Hz}^{0.5} \cdot \mathrm{W}^{-1}$ (at 0.9 V bias, 525 nm) with fall time about 90 µs.[13] Apart from a good jettability and morphology control of printed organic and polymer PD, poor long-term stability, low intrinsic photoconductivity, limited device configuration, and the dispersibility in biocompatible solvents are issues facing the development of organic printed PD.

On the other hand, inorganic PD such as nanowire and nanoparticles demonstrate relatively high photoconductivity (0.4 kHz bandwidth with high internal gain ($G > 6.5 \times 10^3$) than organic printed PD through the controlled introduction of defects. Recently, some inorganic printed PD have been demonstrated, but their performance is not comparable to that of inorganic PD made by other solution coating method because of the low quality of the film.[14] The poor controllability of

fabricating the desired network using inorganic ink via inkjet printing removes its outstanding intrinsic optoelectrical property, and it results in poor device performance (i.e. short lifetime, low response time, little gain), especially with low-temperature manufacturing processes (< 150 °C). Thus, it is necessary to develop a new method to control the printability of inorganic ink for realising a high-performance inorganic printed PD.

Previously, high boiling point solvents have been used for inorganic nanoparticle ink to enhance ink stability and jettability. Despite this, the jettability of the nanoparticles is dependent on the high boiling point solvent system, which is theoretically and experimentally well studied. The practical property, such as the optoelectrical property of the film, is not thoroughly investigated.[15] It is essential to consider the effect of the solvent on the device performance. High boiling solvent residue can affect the physical properties of nano-dimensional inorganic materials. Most studies with nanoparticles demonstrate proper functions following a high-temperature post-annealing process (> 200 °C) or strong UV treatment. Yuhui Dong *et al*., demonstrated that the ZnO NP ink in ethylene glycol/glycol mixture showed only photodetection behaviour after UV treatment.[16] Photo-responsivity is relatively low over the device made by other solution-based coating processes and required high external voltage (60 V) after UV treatment.

Moreover, in the field of flexible electronics and bio-electronics, low boiling point ink is highly desired due to four main advantages.[17] Firstly, fast evaporation of the solvent can reduce the probability of re-dispersion between the layers of the heterostructure, making it possible to diverse the device configuration. Secondly, low solvent residue decreases further damage to active materials and increases operational stability. Thirdly, low boiling point inks have been shown to minimise the 'coffee ring' effect which typically transports flakes to the edge of the deposited film when dried; therefore the morphological uniformity and layered arrangement can be improved.[18-

4

[19] Finally, the lower boiling point solvents (<100 °C) tend to be biologically safer and more economical than high boiling point organic solvent (>100 °C) such as ethylene glycol.[20] However, when a low boiling point inks are used in inkjet printing, they tend to dry around the inkjet nozzle which can cause blockages when used over long periods (days) even when cleaning cycles are applied.

In this study, we have designed a new strategy to create a highly desirable surface morphology with inorganic NP ink using a low boiling point solvent. The NP ink in the co-solvent system with 1) high boiling solvent and low boiling solvent; and 2) two low boiling solvents; are investigated in the aspects of surface morphology and optoelectrical property. Then, the effect of solvent residue and contact junction status on printed electronics are researched. Finally, the microporous structure is constructed to improve the responsivity of PD. This is achieved through maximising the local surface tension differences during the printing, which shows high photoresponsivity ($R_{Maximum}$: $7.5*10^2$ AW^{-1}) with the fast response time.

RESULTS AND DISCUSSION

Ink formulation Figure 1a shows the schematic illustration of the fabrication method for inkjet-printed PD using inorganic ink. Among many other inorganic materials, we chose ZnO NP due to its high quantum efficiency, low cost, stability, high-temperature operation capability, and environmental compatibility.[21] Typically, the high crystalline ZnO NPs were prepared according to a previous report for our photodetector applications.[22] As shown in Figure S1a, the X-ray diffraction pattern for typical hexagonal crystal structures can be resolved. The characteristic peaks of {100, 002, 101, 102, 110, 103} can be readily indexed according to the standard PDF: 80-0075.

The broad diffraction peaks indicate the small crystal domains which are consistent with the high-resolution transmission electron microscopy (HRTEM) images (Figure S1b) and indexed selected-area electron diffraction pattern (Figure S1c).
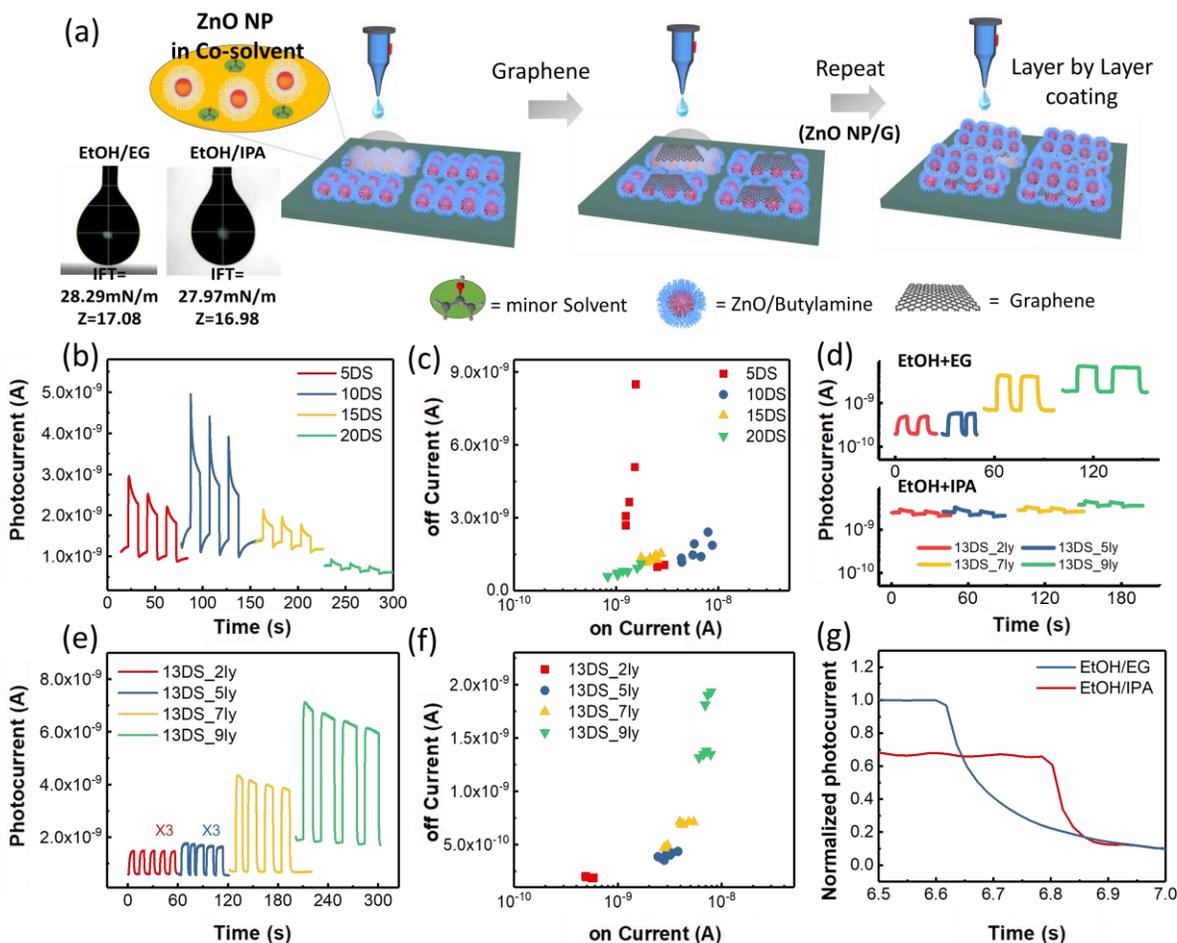
Figure 1. (a) Schematic illustration of the PD printing process using ZnO/Graphene: Inset is interfacial tension of droplets with two cosolvent systems (EtOH/EG and EtOH/IPA) and their corresponding Z values. (b) Transient photocurrent time plot as a function of inkjet drop spacing in EtOH/EG co-solvent system with 18°C platen temperature. (c) On and off current distribution depending on inkjet drop spacing (DS): 5 DS, denotes 5 drop spacing. (d) Transient photocurrent time plot as a function of printing cycles for EtOH/EG ink with 40 °C platen temperature. (e)

6

Transient photocurrent time plot as a function of the printing cycle (ly) in EtOH/EG co-solvent system with 40 °C platen temperature; 13DS-2ly, denotes 13 um drop spacing with 2 layers printing. (f) On and off current distribution depending on the printing cycle. (g) Photoresponse time for EtOH/EG and EtOH/IPA ink.

For a printed PD, Ag reactive ink is printed first, and photoactive material is printed on the top of the electrode to build a planer architecture PD. To improve the detectivity of printed ZnO NP based PD, the graphene flake and ZnO NP is deposited layer by layer. The ethanol, which is biocompatible, is chosen as a primary low boiling solvent to estimate the jettability and controllability of ZnO NP ink. Due to the low boiling point solvent rapidly drying around the nozzle during the inkjet printing, we have designed co-solvent systems with ethanol for the low boiling point ink for the inorganic ink. Either ethylene glycol (EG) or isopropanol (IPA) is used as a minor solvent. We estimate the jettability of each ink and engineer them to be within the optimal Z range (2< Z <24, $Z=Oh^{-1} = (\gamma \rho a)^{1/2}/\eta$) before printing.[23] The inverse Ohnesorge number (Oh) is used as a figure of merit. Several important parameters including the ink viscosity η, surface tension γ, density ρ, and the nozzle diameter, a (=21 μm) influence the jetting of individual drops from a nozzle.[24-25] In case of cosolvent ink, the degree of viscosity, surface tension, and vapor pressure are the terms affected by mixing friction of two solvents, so it is possible to modulate the Z value of our ink through changing the mixing ratio between them;

$\gamma_{mix} = \sum_i^n x_{i,s}\gamma_i,$ ($x_{i,s}$ is mole fraction, γ_i is the surface tension of each solvent) …. (1)

$\eta_{mix} = \exp\left(\exp\left(\frac{(\sum_i^n x_i VBN_i)-10.975}{14.534}\right)\right) - 0.8,$ …. (2)

$VBN_i = a * \ln\left(\ln(\eta_i + 0.8)\right) + b$ …. (3)

(x_i is mass friction, a, b is constant, η_i is the kinematic viscosity of each solvent)

$$vp_{mix} = \sum_i^n x_i vp_i, \quad (x_i \text{ is mole fraction, } vp_i \text{ is the vapor pressure of each solvent}) \dots (4)$$

These equations (1) – (4) are based on the ideal case, and it can be modified as a function of the liquid system (thin film, droplet), but each component affected by the frictions will not be changed.[7, 26-27] Thus, we calculate a various ratio of EtOH/EG and EtOH/IPA cosolvent system respectively to obtain the optimum Z value of our inks (Table S1). It appears that 10:1 vol % to 50:1 vol % EtOH/EG and below 5:1 vol % EtOH/IPA shows good jettability among other compositions (Figure S2). The rheological parameters (η, γ, and ρ) of ZnO NP ink is $\eta_{ZnO} \sim 6$ mPa s, $\gamma_{ZnO} \sim 28.29$ mN m^{-1}, $\rho_{ZnO} \sim 0.48$ g cm^{-3}, for 50:1 vol % EtOH/EG and $\eta_{ZnO} \sim 1$ mPa s, $\gamma_{ZnO} \sim 27.97$ mN m^{-1} for 5:1 vol % EtOH/IPA and its correlated Z value is 3.4 for 50:1 vol % EtOH/EG and 16 for 5:1 vol % EtOH/IPA, which is in the optimum Z range (Figure 1a inset, Figure S2). Owing to good jettability of inks, we can make a fine pattern using EtOH/EG and EtOH/IPA ink while ZnO NP in EtOH shows poor line patterning due to satellite formation (Figure S3a, b)

ZnO NP printed PD. We fabricate a printed PD using ZnO NP in EtOH/EG and ZnO NP in EtOH/IPA to investigate the solvent effect on the optoelectrical property of ZnO NP. EG is chosen as a high boiling point solvent, and IPA is chosen as a low boiling point solvent. Before investigating the solvent effect, photo-responsivity is tuned through the drop spacing and the number of printing cycles using the EG/EtOH ink. Figure 1b shows the highest responsivity with 10 μm drop spacing under the same number of printing cycles. Despite the film with 5 μm drop spacing containing twice the amount of ZnO NP than the 10 μm film, the 5 μm film shows lower responsivity because a larger amount of high boiling point EG has remained during printing and has increased the coffee ring effect (Figure S4a-c).

Moreover, performance repeatability is poor with narrow drop space printing. The film with 15 μm drop spacing has the smallest deviation of device performance among others (Figure 1c). Therefore, a 13 μm drop spacing is adapted for both EtOH/EG and EtOH/IPA ink experiments. Interestingly, all PD made by EtOH/EG ink demonstrate slow response time, large dark noise level, and fast accumulation - recombination behaviour. Without any post-annealing process, the high boiling point EG remains in the film, and it impedes the charge transport of photogenerated carriers. Thus, photogenerated charge carriers are accumulated and spontaneously recombined at the junction between the ZnO NPs film made by EtOH/EG ink. Therefore, the photocurrent drastically decreases despite the continuous light exposure. FT-IR spectroscopy clearly indicates a large amount of carbon residual with EtOH/EG ink, compared to EtOH/IPA ink without any annealing process (Figure S4c). The C-C stretching, O-H stretching, C-O stretching are only detected for EtOH/EG ink printed devices. After using a 40 °C platen temperature and 150 °C post-annealing process for EtOH/EG ink, a large dark noise level, and fast accumulation - recombination behaviour is reduced in Figure 1d and e, owing to the reduced solvent residue. Also, photo-responsivity with different printing cycles are studied. The responsivity of the device is proportionally increased with the increased number of printing cycles due to high absorption, but the dark current, response time and the repeatability of the device somewhat decreases after 9 printing cycles due to the colloidal aggregation during printing (Figure1e, f). Finally, we fabricate a device with a 13 μm drop spacing with 7 layers of printing for both ZnO NP in EtOH/EG and ZnO NP in EtOH/IPA (Figure 1g). The EtOH/EG ink shows a higher I_{light}/I_{dark} ratio (11 at 405 nm 1mW) than EtOH/IPA ink (2 at 405 nm 1 mW), but the rising time and falling time of the EtOH/IPA ink is 4 times higher than that of EtOH/EG ink (Figure 1e and 1g). Unlike the EtOH/IPA ink, which has a similar surface tension between two solvents, EtOH/EG ink has a larger difference

in their surface tension so that the EtOH/EG ink formed a more porous and rougher surface than EtOH/IPA ink. Atomic-force microscopy (AFM) analysis shows that many pores between 200 nm to 1 μm exist in the film which is printed via EtOH/EG ink, in contrast to the smooth thin film which is printed from EtOH/IPA ink (Figure S4d, e). The higher porosity of EtOH/EG ink improved the PD performance due to the increased absorption of UV light within the porous structure. The film printed from EtOH/EG ink showed twice the absorption at 360 nm - 400 nm region than the film which was printed from the same amount of EtOH/IPA ink (Figure S4f). Due to the different porosity between the two films, a more significant PD I_{light}/I_{dark} ratio is obtained with EtOH/EG ink. Although the surface morphology of EtOH/EG ink printed films are optimised through controlling the drop space, printing cycle, and annealing process, inferior device performances remain (i.e. the response time, accumulation - recombination behaviour). We believe that the high boiling point EG which remains after the annealing process (< 100 °C) is the origin of the poor device's performance.

Microporous ZnO NP/Graphene via inkjet. To improve photo-detectivity from as-printed ZnO films, we design a new approach to modulate the porosity of film using a mixing low-boiling point cosolvent (EtOH/IPA) system as shown in Figure 2a. The microporous structure of EtOH/EG ink is driven by 'Bénard – Marangoni' convection flow effect. Evaporation-driven surface tension gradient in the liquid layer can cause the convective flow, and it generates a specific pattern on the surface. Microporous structure formation by Bénard − Marangoni convection has been introduced in spin coating[28] and dip coating[29] approaches. For instance, Hiroaki et al. demonstrated the spontaneous porous pattern formation using cosolvents with high surface tension and low volatility (e.g. 2-propanol with dipropylene glycol using the dip-coating method).[29] Inkjet-printed films have also been known to be affected by the Bénard − Marangoni convection.[30] Improper Bénard

− Marangoni convection results in a coffee ring effect in the inkjet method. Thus, enhancing the Bénard − Marangoni convection during inkjet printing can construct the microporous film analogous to the dip-coating process, which shown by our EtOH/EG ink in this study. The initial state of a droplet is similar between EtOH/EG (volatile solvent with high surface tension solvent) and EtOH/IPA (volatile solvent with low surface tension solvent), while fluidic behaviour between them have a huge difference. While the droplet reaches the transition zone, EtOH/EG undergoes the Bénard − Marangoni convection due to different gas-liquid surface tension of EG, compared to EtOH and IPA and it results in the porous structure. However, residual EG disrupts the photo-response time so that another strategy to modulate the porosity is required.
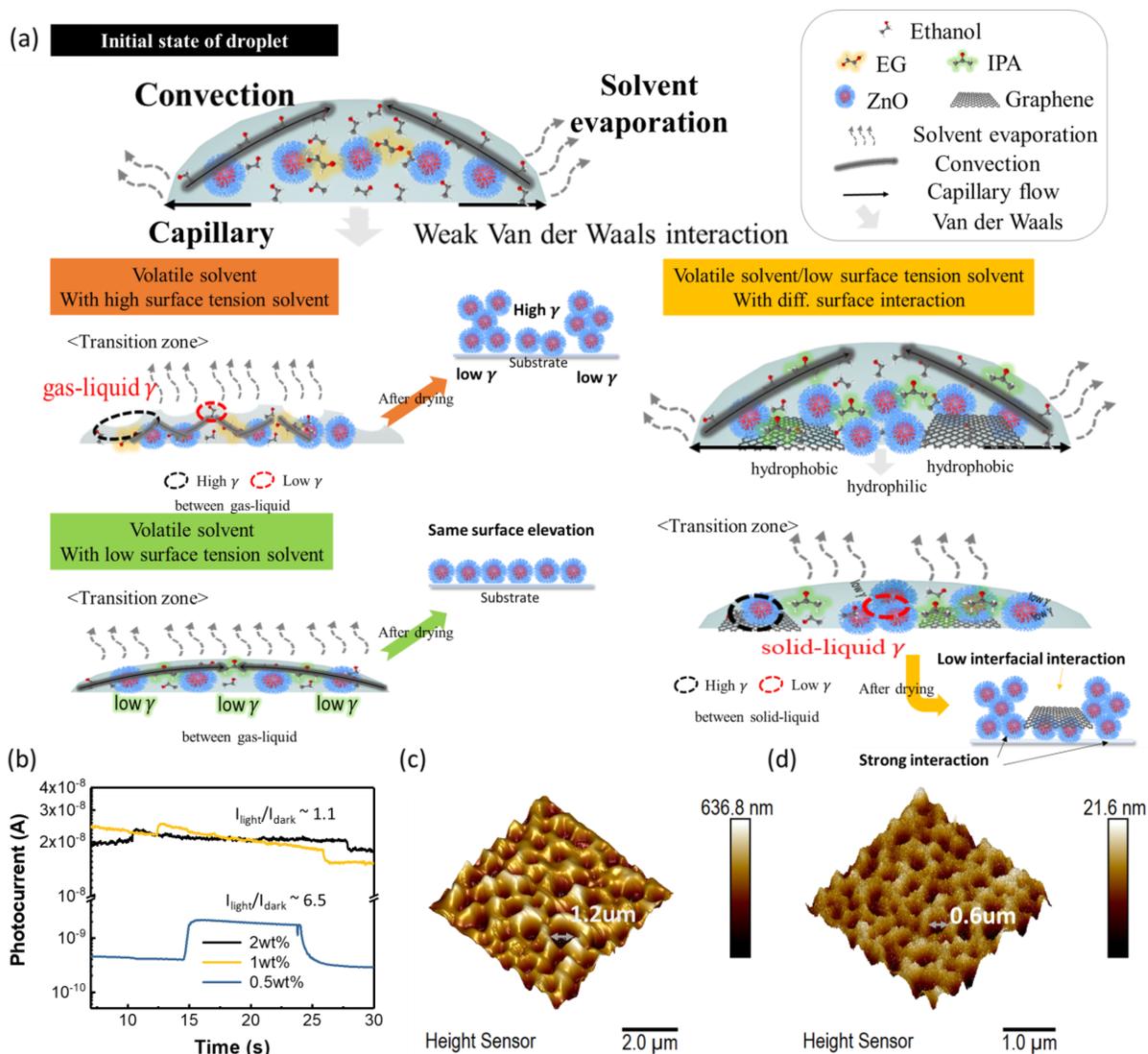
Figure 2. (a) Schematic illustration of hydrodynamic behaviour depending on the ink formula: volatile solvent with high surface tension solvent (EtOH/EG), volatile solvent with low surface tension solvent (EtOH/IPA), volatile–low surface tension solvent with different surface interaction (ZnO in EtOH/IPA with G/EtOH). (b) Photocurrent versus times depending on graphene mass fraction. (c-d) AFM image of layer-by-layer printed ZnO/G film with ZnO in EtOH/1-propanol and graphene in EtOH (c) and with ZnO in EtOH/IPA and graphene in EtOH (d).

In a low - low boiling point system, we facilitate the Bénard − Marangoni convection through differentiating the surface tension using graphene flake. The Bénard − Marangoni convection can be characterised by the Marangoni number, M_a:[31]

$$M_a = \frac{-(\partial\gamma/\partial T)H^2\,\nabla T}{\mu\alpha} = \frac{-(\partial\gamma/\partial C)H^2\,\nabla C}{\mu D} \qquad\qquad \text{.......} \quad (4)$$

where $\partial\gamma/\partial T$ is the temperature derivative of the surface tension, $\partial\gamma/\partial C$ is the concentration derivative of the surface tension, H is the thickness of the solution layer, μ is viscosity, α is thermal diffusivity of the solution, D is the mass diffusivity of the component, and ∇T and ∇C are the temperature and concentration gradient near the solution surface, respectively, because the Bénard − Marangoni convection occurs when M_a is high. The M_a can be enlarged when increasing temperature or increasing concentration gradients or increasing thicknesses. Lowering the viscosity can also assist in creating a microporous pattern with low-low boiling point solvent. We cannot manipulate the temperature factor within inkjet printing due to the use of a low-low boiling solvent which would induce clogging issues, while concentration derivative and mass diffusivity can be well controlled by differentiating the underlying materials.

Therefore, we have used graphene flakes to generate surface tension instead of using a high boiling point solvent, which is EG for the co-solvent system, in a low boiling point co-solvent system. The Graphene is synthesized via the solvent exfoliation method and re-dispersed in EtOH, followed by our previous paper[40] so that the physical property of graphene will be same. A solid-liquid surface tension variation can be created between the hydrophobic graphene and hydrophilic ZnO NP which can lead to ZnO/Graphene microporosity network via inkjet printing. The graphene flake and ZnO NP are deposited layer by layer to enhance the Bénard – Marangoni effect. Firstly, we optimised the mass friction between ZnO NP and Graphene for PD devices. Graphene is a highly electrically

conductive material. A small amount of graphene can improve PD performance by reducing contact junction resistance between ZnO NPs. However, a large amount of graphene will induce a fully conductive channel,[32] which is not desirable for PDs. As shown in Figure 2b, a different mass fraction between graphene and ZnO NP exhibit different photo-responsivity (Figure 2b). For instance, the 2 wt% and 1 wt% graphene insertion on the ZnO film shows a higher dark current and smaller I_{light}/I_{dark} ratio than the pure ZnO film. Based on photo-responsivity as a function of graphene/ZnO ratio, we found 0.5 wt% graphene on ZnO film shows the best PD performance. When the graphene concentration increases over 1 wt%, the dark current is increased due to the conductive nature of graphene and the photoresponse is decreased due to intermolecular energy transfer between graphene and ZnO NP. Therefore, it is an effective strategy that the porosity is modulated by a solvent system with a fixed graphene concentration.

The surface morphology of ZnO NP/graphene is examined with various cosolvent systems. When the low volatile cosolvent with lower surface tension is mixed (EtOH/1-Butanol), the low volatile solvent evaporates together with the solutes during the EtOH evaporation.[33] Therefore, the generation of pinholes is successfully suppressed to 100 - 200 nm size regardless of surface tension differences between ZnO and graphene (Figure S5). We believe butanol which has a longer alky chain than ethanol can decrease surface tension difference between ZnO and graphene, which results in the stronger interaction between residual butanol and graphene. On the other hand, ZnO NPs in EtOH/1-propanol and EtOH/IPA demonstrate delicate microporous patterns via layer-by-layer printing with graphene (Figure 2c, d). The AFM image of ZnO/graphene film using EtOH/1-propanol (Figure 2c) indicates over 1 μm size holes were generated with 282 nm RMS in a 5 μm x 5 μm area, while the ZnO/graphene film using EtOH/IPA (Figure 2d) shows approximately 600 nm size holes were generated with 13 nm RMS in a 5 μm x 5 μm area. The higher surface tension

from 1-propanol over IPA facilitates random fluctuations in local surface tension and causes lateral fluid motion, resulting in the more significant regional surface tension differences.

As well as this, 1-propanol has higher vapor pressure and lower viscosity than 1-Butanol, which results in a microporous film structure during the fast evaporation. It should be noted that the surface tension differences mainly induced by graphene flake, and the minor solvent should not actively interact with the graphene flake. Fast evaporation cosolvent systems only affect the microporous pattern formation induced by the Bénard−Marangoni convection with the ZnO/graphene network.

A detailed investigation was conducted as a function of the co-solvent mixing ratio. The AFM images indicate no porous structure with ZnO NP in EtOH (Figure 3a) and ZnO NP in IPA (Figure 3b). Regardless of the mixing ratio between EtOH and IPA, we found the ZnO NP ink shows a small porosity, which gives a lower PD response because of small differences in the surface tension (Figure 3a-c). Figure 3d-f shows the surface morphology of ZnO film on the top of graphene flake film (2 cycles of ZnO printing on 1 cycle of graphene printed film). We found by just simply coating ZnO on the graphene film can result in a porous structure. The film which was printed using ZnO NP in 10:1 EtOH/IPA (Figure 3d) shows 30 – 80 nm pinholes with a large surface roughness (RMS over 98 nm). The number of holes in this film dramatically increased compared to that of ZnO only films, and we have found the number of the pores monoclinic increased as a function of EtOH adding ratio. A monodispersed pinhole (approximately 100 nm) is obtained in ZnO/graphene film which is printed through dispersing ZnO NP in 5:1 EtOH/IPA. This also creates a fine surface morphology due to the rapid evaporation and low viscosity (Figure 3e). However, the films printed from ZnO NP in 1:5 EtOH/IPA (Figure 3f) ink solution presents a large difference in thickness (RMS over 114 nm) with inhomogeneous pinholes, unlike EtOH dominant

co-solvent system. The rapid solvent evaporation during the printing process is the key factor to provide the concentration gradation of the solutes, which generates a local higher surface tension as a result of different intermolecular interactions. Finally, we achieve the precise control of the hole size from ZnO/graphene layer-by-layer printing, as shown in Figure 3g-i. We use a 5:1 EtOH/IPA solvent to ascend the number of holes in ZnO/graphene film, and the hole size is controlled by using different concentration of graphene inks. For instance, the 0.1 mg/mL, 0.2 mg/mL, 0.4 mg/mL graphene solution create a well-packed printed film with below 100 nm hole (Figure 3g), 200 – 500 nm hole (Figure 3h), 1 μm hole (Figure 3i), respectively. Furthermore, we prepared cross-section specimens via FIB milling for direct analysis of the morphology of ZnO/graphene film. As shown in Figure S6, graphene intercalated ZnO film can be readily observed through the high-resolution TEM analysis, which matches with our understanding. The layer-by-layer printed ZnO/Graphene using the high boiling point solvent show stacked film configuration between ZnO and graphene while layer-by-layer printed ZnO/Graphene using low boiling point solvents exhibit microporous structure.
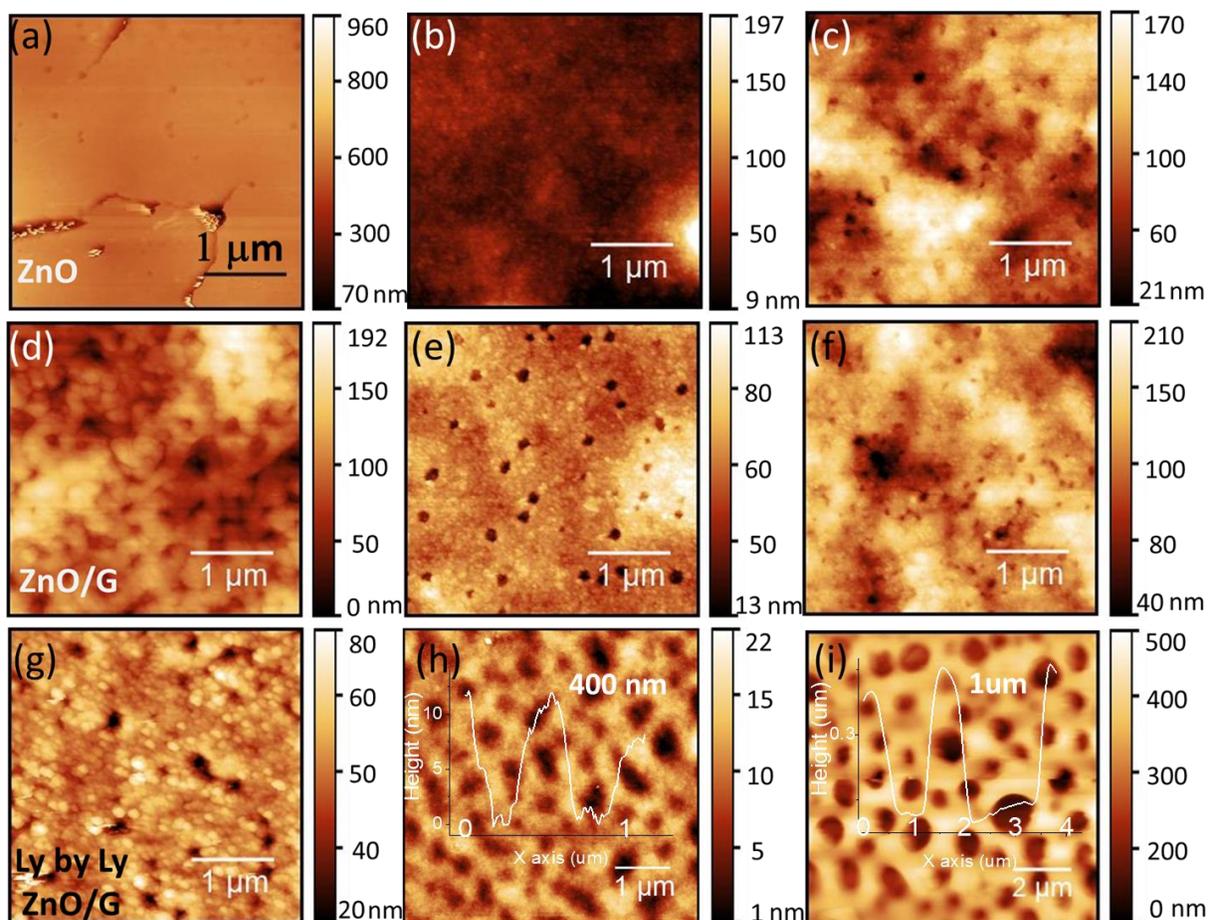
Figure 3. (a-c) AFM image of ZnO film depending on different EtOH/IPA volume ratio: EtOH (a), 5:1 EtOH/IPA (b), IPA(c). (d-f) AFM image of ZnO film on the top of printed graphene surface depending on different EtOH/IPA volume ratio: 10:1 EtOH/IPA(d), 5:1 EtOH/IPA (e), 1:5 EtOH/IPA (f). (g-i) AFM image of layer by layer printed ZnO (in a 5:1 EtOH/IPA)/Graphene film using depending on different graphene friction: 0.1 mg/mL (g), 0.2 mg/mL (h), 0.4 mg/mL (i). ZnO/graphene printing sequence is same for (g)-(i); graphene (1 layer)/ZnO (2 layer)/ graphene (1 layer)/ZnO (2 layer)/ graphene (1 layer)/ZnO (3 layer)

Printed PD performance. The photodetectivity of as prepared layer-by-layer ZnO/graphene PD are systematically studied to understand the correlation between surface morphology and the

17

optoelectrical property of ZnO NP. Due to the porous structure, the I_{light}/I_{dark} ratio of ZnO/graphene PD drastically increased compared to I_{light}/I_{dark} ratio of ZnO film (Figure 4a-c). Interestingly, we found the response time and I_{light}/I_{dark} ratio of PD is profoundly affected by the size of porosity and surface roughness. Under 1mW 405 nm light irradiation, the layer-by-layer ZnO/graphene PD printed from EtOH/1-propanol show an I_{light}/I_{dark} ratio of 16 with 10 s fallen time and ~10 s rise time (Figure 4a). The I_{light}/I_{dark} ratio and response time decrease noticeably after the annealing process, this may occur due to the large porosity (1 μm) and the high surface tension difference between ZnO and graphene. A more significant porosity of the printed film indicates the formation of a larger ZnO colloidal aggregation which indicates the poor response time has originated from the inferior contact junction between each ZnO NPs due to the nanoscale graphene not sufficiently bridging these voids (Figure 4d, Figure S7a).

On the other hand, the layer-by-layer printed ZnO/graphene PD using EtOH/IPA cosolvent system shows an 8 I_{light}/I_{dark} ratio with 0.18 s rise time and 4 s fallen times (1mW 405 nm light exposure, Figure 4b). After the annealing process, not only does the I_{light}/I_{dark} ratio enhances to 13.6 but also maintains the rise time at 0.22 s. Based on height analysis, the microscopic surface roughness of EtOH/IPA ink printed film is much smaller than EtOH/1-propanol (100 μm x 100 μm, Figure 4e, Figure S7b), which suggest uniform graphene and ZnO deposition with porous structure can significantly enhance photoresponsivity with fast photo-response time.
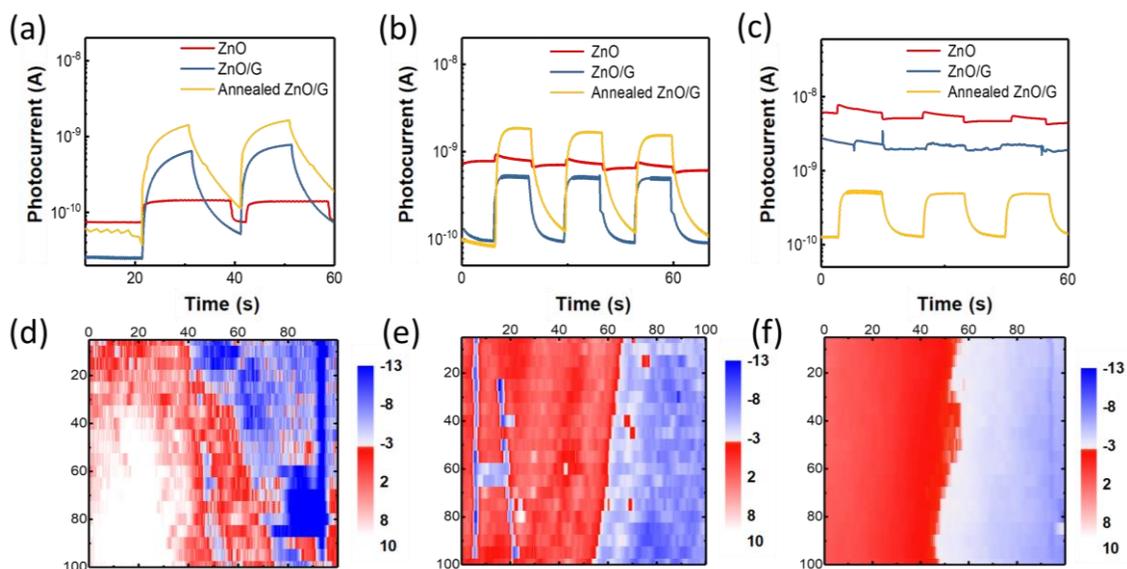
Figure 4. (a-c) Under 1 mW 405 nm irradiance, transient photocurrent plots of ZnO, layer-by-layer printed ZnO/G and annealed ZnO/G film for ZnO in EtOH/1-propanol (5:1) with Graphene in EtOH (a), ZnO in EtOH/IPA (5:1) with Graphene in EtOH (b), ZnO in EtOH/IPA (5:1) with Graphene in DMF (c). (d-f) Height mapping for corresponding films: ZnO in EtOH/1-propanol (5:1) with Graphene in EtOH (d), ZnO in EtOH/IPA (5:1) with Graphene in EtOH (e), ZnO in EtOH/IPA (5:1) with Graphene in DMF (f).

To verify our hypothesis, we print a uniform graphene and ZnO film without a porous structure by dispersing graphene in dimethylformamide (DMF). Generally, DMF is a high boiling solvent which can hinder the evaporation during the printing process. Uniform and non-porous layer-by-layer ZnO/graphene films are also obtained when we employ the ZnO NP in EtOH/IPA solution (Figure 4f, Figure S7c). However, due to the large DMF residual, PD performance is inferior. Even after the annealing process, I_{light}/I_{dark} ratio (around 7) of layer-by-layer printed ZnO/graphene PD is still lower than the aforementioned porous structure (Figure 4c).

Table 1 demonstrated the PD performance depending on the solvent system with and without graphene. When the co-solvent system is changed, the porosity of the film is changed, and when the porosity is changed, I_{light}/I_{dark} ratio is changed. The high boiling point solvent which remains even after the annealing process (< 100 °C) demonstrated inferior photoresponse time compared to low boiling point co-solvent system since carbon residue hinders the transport of photocarrier between ZnO NP. Porous structure also can be generated via graphene/ZnO NP. Even after one-layer printing of ZnO on graphene, we can observe the porous structure. Fig. S8 is the one-layer printing of ZnO for the same condition with Fig. 3e. When the number of printing is increased, the porosity becomes discrete and uniform, which means there is a templating effect. However, the size of the porosity is more or less the same. The pore size of the graphene/ZnO NP structure can be tuned through graphene concentration and solvent type (~ 1 um to 100 nm). Even though the micro-porous structure is obtained with high graphene concentration, the PD performance is poor compared to similar microporous structure generated by EG/EtOH system due to the conductive nature of graphene.

Table 1. Comparative table for photodetector performance in this work. The optimal parameters result in the champion devices are also highlighted in the table. The red color is representative data to show discrete PD performance changes depending on the solvent system and graphene insertion.

Material	Solvent	DS/layer	I_{light}/I_{dark} (405nm)	t (fallen)	Pore size
ZnO	EtOH	13/5	Not reproducible		Cracked thin film
	IPA	13/5	Not reproducible		Thin film
	EtOH/IPA 5:1 vol%	5/2	2.45	0.77	Thin-film with few pinholes
		10/2	3.16	0.33	Thin-film with few pinholes
		15/2	1.55	0.32	Thin film
		20/2	1.18	0.49	Thin film

		13/2	1.20	0.25	Thin film
		13/5	1.39	0.56	Thin film
		13/7	**2.02**	**0.55**	**Thin film**
		13/9	1.22	0.39	Thin film
	EtOH/EG 50:1 vol%	5/2	2.36	3.90	Microporous ~1um
		10/2	3.10	1.25	Microporous ~1um
		15/2	6.17	2.66	Nano-Microporous
		20/2	3.82	3.01	Nano-Microporous
	EtOH/EG 50:1 vol% (40 °C)	13/2	2.42	2.41	Nano-Microporous
		13/5	3.00	2.21	Nano-Microporous
		13/7	**11.1**	**2.22**	**Nano-Microporous**
		13/9	4.21	2.25	Nano-Microporous
ZnO/G_2wt%	EtOH/IPA	13/2 +1G	1.16	0.6	Microporous (1 um)
ZnO/G_1wt%	EtOH/IPA	13/2+1G	1.15	0.4	200 – 500 nm
ZnO/G_0.5wt%	EtOH/IPA=10:1	13/2+1G	-	-	30 – 80 nm
	EtOH/IPA =5:1	**13/2+1G**	**6.50**	**1.03**	**Uniform 100 nm**
	EtOH/IPA=1:5	13/2+1G	-	-	Thin film with few pinhole
	EtOH/BuOH	13/2+1G	-	-	Inhomogenous nanopore
ZnO/G Layer by layer	EtOH/PrOH	13/7+3G	16	10	Microporous (1.2 um), RMS↑
	EtOH/IPA	13/7+3G	8	4	Nanoporous (600 nm) RMS↓
	EtOH/IPA (annealed)	13/7+3G	13.6	9.82	Nanoporous (600 nm)
	EtOH/IPA (7 fingers)	**13/7+3G**	**14.4 6*10⁴ (365nm)**	**9.22 2.4**	**Microporous**

To improve and demonstrate the reliability of our printed UV PD, three parallel-connected seven fingered channel is fabricated (optical microscopy image is shown as Figure S9). Due to the inherent microstructures from as-prepared integrated electrodes (100 μm *800 μm / L*W), the

microporous size of layer-by-layer printed ZnO/graphene PD (EtOH/IPA ink) is changed from 500

nm to 1 μm (Figure 5a). Owing to the well-controlled porosity, as-prepared integrated UV PD

demonstrates remarkable performance. A 14.4 I_{light}/I_{dark} ratio can be achieved under 1mW 405nm

light irradiation, and a $6*10^4$ I_{light}/I_{dark} ratio can be obtained under 0.5 mW 365nm light exposure.

Moreover, three parallel-connected seven fingered channel show an average $4*10^4$ I_{light}/I_{dark} ratio

compared to 150 I_{light}/I_{dark} ratio from one-fingered channel among 20 devices (Figure 5b, c).
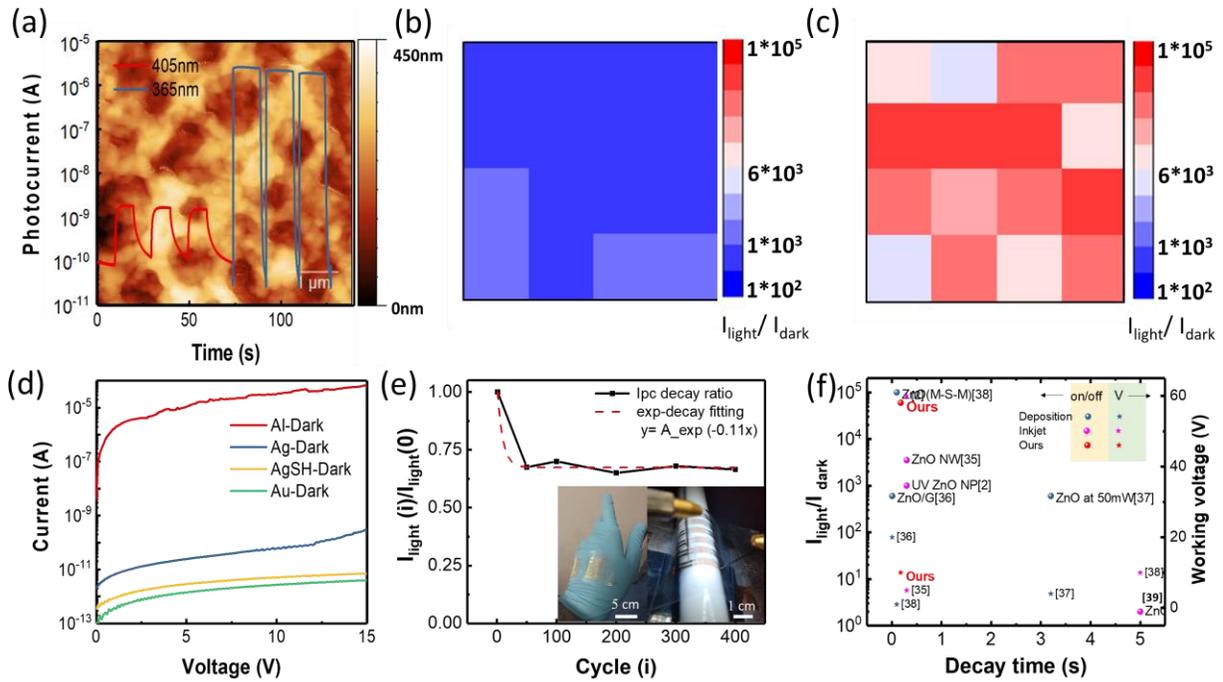

Figure 5. (a) Transient photocurrent plot for layer-by-layer printed ZnO/G on seven finger

channels under different irradiance wavelength. The background is the corresponding AFM image

of the film. (b-c) I_{light}/I_{dark} ratio distribution profile of PD devices with single-channel devices (b)

and multi-channel devices (c). (d) Voltage - current plot without light exposure depending on the

channel electrode: Al (Al), printed Ag (Ag), printed Ag with surface functionalization (AgSH),

and Au (Au) electrode. (e) Flexible durability test for printed ZnO PD and inkjet-printed flexible

integrated sensor networks (inset). (f) I_{light} /I_{dark} ratio and response time plot for previous studies and our works.[35-39]

We use e-beam evaporation to deposit Al and Au electrode to understand the effect of work function on devices since the Schottky contact with channel and electrode can induce a low dark current. We found the Al-based electrode PD shows a higher dark current while the Au electrode shows a lower dark current (Figure 5d). This means Al has Schottky contact with ZnO while Au is ohmic contact. To modulate the work function of the printed Ag electrodes, we modify the Ag electrodes surface with a thiol derivative.[7] After thiol modification on the printed Ag electrode, the dark current is mostly reduced. As a result, final PD demonstrates maximum responsivity around $7.5*10^2$ AW^{-1} and average $6.2*10^2$ AW^{-1} for ten devices with average I_{light}/I_{dark} ratio around $4*10^4$, which is an outstanding detectivity compared with other report printed ZnO PDs (Figure 5e).

Furthermore, the as-printed PDs also show excellent flexible durability. As shown in Figure 5f, an $\varepsilon = 0.8$ tensile strain is applied to the PD devices, and the photo-responsivity change is monitored as a function of bending cycles. During the initial stage (up to 40 cycles of the flexible test), I_{light}/I_{dark} ratio of device drastically decrease due to crack propagation which is well-known phenomena for flexible devices. After 40 cycles, PD performance becomes stable, which is consistent with the typical sliding behaviour of channel materials.[34] Encouragingly, the as-printed flexible PD shows robust performance even after 400 cycles of bending tests.

CONCLUSIONS

In summary, we propose a new approach to modulate the surface morphology of the inkjet-printed nanoparticle film via using a low boiling point cosolvent ink solution. A volatile solvent is used as the primary solvent to facilitate the evaporation of the solvent during the inkjet printing. To reduce the clogging, the volatile solvent is mixed with a high boiling point solvent. The porous structure is obtained using both gas-liquid surface tension differences and solid-liquid surface differences, and the size of porosity is modulated from nano-size to micro-size depending on the ratio between two solvents or two nanomaterials. The surface morphology and the PD performance are summarized in Table 1. Depending on the surface tension of the minor solvent or minor material, the surface morphology can be altered from a smooth thin film to nanoporous or micro-porous film. The thin-film demonstrates low I_{light}/I_{dark} ratio, but fast photo-response time. When the porosity increases, I_{light}/I_{dark} ratio increases because the absorption of UV light is increased within the porous structure. Moreover, the small amount of graphene improves PD performance by reducing contact junction resistance between ZnO NPs.

EXPERIMENTAL METHODS

Inkjet Printing. A drop-on-demand inkjet printer (Fujifilm Dimatix DMP-2800) equipped with a 21 µm diameter nozzle (Fujifilm DMC-11610) was used, and the volume of individual droplets from the nozzle is controlled at ~10 pL during our printing process. The platen temperature was kept at room temperature (<20 °C) throughout the printing of the heterostructures. Each ink was printed at a maximum jetting frequency of 2 kHz. The polyethylene naphthalate (PEN) film (Teonex®) is used for PD substrate due to good surface roughness. The patterned channel electrodes are formed via printing Ag ink (jet-600C, supplied by Hisense Electronics, Kunshan,

China) on a PEN substrate at a drop spacing of 50 μm and then annealed at 130 °C for 30 min. Then, the ZnO NP ink (25 mg/mL in specific solvent) is printed at a drop spacing of 13 μm with a single nozzle jetting. Subsequently, the Graphene NP ink is printed at a drop spacing of 40 μm with a single nozzle jetting. The Graphene printing is repeated every two printing cycles after each ZnO ink printing cycle. The film is dried at room temperature in a vacuum desiccator. Followed by the previous study.[7] the work function modulation of Ag electrode is realised through applying perfluorobenzenethiol (PFBT)-ethanol solution (PFBT : ethanol = 1:1000) on the Ag electrode for 3 min and then rinsed with ethanol.

Photodetectivity. Detectivity and photoresponsivity are calculated as a figure of merit for photo-detection performance via the following equation.[37]

$$\text{Photoresponsivity } (R_i) = \frac{(I_{light} - I_{dark})}{P_{opt}}$$

$$P_{opt} = P_0 dL \ (P_0 = incident\ power\ density)$$

ASSOCIATED CONTENT

Supporting Information.

The detail information about material characterization methods; XRD, TEM, SAED analysis results of ZnO NPs (Figure S1); detail description about ink solution characterisation methods and Z value for every ink formula (Table S1); the viscosity analysis of ink solutions (Figure S2); and optical images (Figure S3), FTIR (Figure S4), AFM (Figure S3 and Figure S4), UV-VIS absorption spectroscopy (Figure S5) of different types of ink solutions and printed line patterns; TEM cross-

section image of printed thin films (Figure S6); the detail information of device preparation and characterisation methods; SEM (Figure S7) and AFM images (Figure S8) of as-printed thin films; and optical microscopy images of the as-prepared photodetector and corresponding equivalent circuit design (Figure S9).

AUTHOR INFORMATION

Corresponding Author

E-mail: sh977@cam.ac.uk (S.D.H.).

E-mail: HouB6@cardiff.ac.uk (B.H.).

ORCID:

Hanleem Lee: https://orcid.org/0000-0003-0958-6514

Bo Hou: https://orcid.org/0000-0001-9918-8223

Author Contributions

H.L. and B.H. conceived the experiments and led the project. H.L. performed inkjet printing and device fabrication. B.H. performed material synthesis and microscopy analysis. S.D.H., S.Y.B., S.L. conducted the e-beam deposition. W. H. C., B. L., S. Z., H.W.C assisted the device fabrication and sample characterization. L.G.O and J.M.K. provided research infrastructure support. H.L. and B.H. wrote the manuscript.

Notes

The authors declare no competing financial interest.

ACKNOWLEDGEMENT

ABBREVIATIONS

NP nanoparticle, PD photodetector, ZnO zinc oxide, EG ethylene glycol, IPA isopropanol, DMF dimethylformamide, Au gold, Al aluminium, RMS root mean square, TEM transmission electron microscopy, FIB Focused ion beam, AFM atomic force microscopy.

REFERENCES

1. Oliveira, J.; Brito-Pereira, R.; Gonçalves, B. F.; Etxebarria, I.; Lanceros-Mendez, S. Recent developments on printed photodetectors for large area and flexible applications. *Org. Electron.* **2019,** *66*, 216-226

2. Gao, M.; Li, L.; Song, Y., Inkjet printing wearable electronic devices. *J. Mater. Chem. C* **2017,** *5* (12), 2971-2993.

3. Kwon, J.; Takeda, Y.; Fukuda, K.; Cho, K.; Tokito, S.; Jung, S., Three-Dimensional, Inkjet-Printed Organic Transistors and Integrated Circuits with 100% Yield, High Uniformity, and Long-Term Stability. *ACS Nano* **2016,** *10* (11), 10324-10330.

4. Kang, Y. J.; Bail, R.; Lee, C. W.; Chin, B. D., Inkjet Printing of Mixed-Host Emitting Layer for Electrophosphorescent Organic Light-Emitting Diodes. *ACS Appl. Mater. Interfaces* **2019,** *11* (24), 21784-21794.

5. Huang, C.-C.; Kao, Z.-K.; Liao, Y.-C., Flexible Miniaturized Nickel Oxide Thermistor Arrays via Inkjet Printing Technology. *ACS Appl. Mater. Interfaces* **2013,** *5* (24), 12954-12959.

6. Jung, S.; Sou, A.; Banger, K.; Ko, D.-H.; Chow, P. C. Y.; McNeill, C. R.; Sirringhaus, H., All-Inkjet-Printed, All-Air-Processed Solar Cells. *Adv. Energy Mater* **2014,** *4* (14), 1400432.

7. Liu, Y.; Li, F.; Xu, Z.; Zheng, C.; Guo, T.; Xie, X.; Qian, L.; Fu, D.; Yan, X., Efficient All-Solution Processed Quantum Dot Light Emitting Diodes Based on Inkjet Printing Technique. *ACS Appl. Mater. Interfaces* **2017,** *9* (30), 25506-25512.

8. Jiang, C.; Choi, H. W.; Cheng, X.; Ma, H.; Hasko, D.; Nathan, A., Printed subthreshold organic transistors operating at high gain and ultralow power. *Science* **2019,** *363* (6428), 719-723.

9. Adly, N. Y.; Bachmann, B.; Krause, K. J.; Offenhäusser, A.; Wolfrum, B.; Yakushenko, A., Three-dimensional inkjet-printed redox cycling sensor. *RSC Adv.* **2017,** *7* (9), 5473-5479.

10. Huber, B.; Popp, P. B.; Kaiser, M.; Ruediger, A.; Schindler, C., Fully inkjet printed flexible resistive memory. *Appl. Phys. Lett* **2017,** *110* (14), 143503.

11. Jin, Y.; Wang, J.; Sun, B.; Blakesley, J. C.; Greenham, N. C., Solution-Processed Ultraviolet Photodetectors Based on Colloidal ZnO Nanoparticles. *Nano Lett.* **2008,** *8* (6), 1649-1653.

12. Singh, M.; Haverinen, H. M.; Dhagat, P.; Jabbour, G. E., Inkjet Printing—Process and Its Applications. *Adv. Mater* **2010,** *22* (6), 673-685.

13. Azzellino, G.; Grimoldi, A.; Binda, M.; Caironi, M.; Natali, D.; Sampietro, M., Fully Inkjet-Printed Organic Photodetectors with High Quantum Yield. *Adv. Mater* **2013,** *25* (47), 6829-6833

14. Deka Boruah, B., Zinc oxide ultraviolet photodetectors: rapid progress from conventional to self-powered photodetectors. *Nanoscale Adv.* **2019,** *1* (6), 2059-2085.

15. Nallan, H. C.; Sadie, J. A.; Kitsomboonloha, R.; Volkman, S. K.; Subramanian, V., Systematic Design of Jettable Nanoparticle-Based Inkjet Inks: Rheology, Acoustics, and Jettability. *Langmuir* **2014,** *30* (44), 13470-13477.

16. Dong, Y.; Zou, Y.; Song, J.; Li, J.; Han, B.; Shan, Q.; Xu, L.; Xue, J.; Zeng, H., An all-inkjet-printed flexible UV photodetector. *Nanoscale* **2017,** *9* (25), 8580-8585.

17. Withers, F.; Yang, H.; Britnell, L.; Rooney, A. P.; Lewis, E.; Felten, A.; Woods, C. R.; Sanchez Romaguera, V.; Georgiou, T.; Eckmann, A.; Kim, Y. J.; Yeates, S. G.; Haigh, S. J.; Geim, A. K.; Novoselov, K. S.; Casiraghi, C., Heterostructures Produced from Nanosheet-Based Inks. *Nano Lett.* **2014,** *14* (7), 3987-3992.

18. Sliz, R.; Lejay, M.; Fan, J. Z.; Choi, M.-J.; Kinge, S.; Hoogland, S.; Fabritius, T.; García de Arquer, F. P.; Sargent, E. H., Stable Colloidal Quantum Dot Inks Enable Inkjet-Printed High-Sensitivity Infrared Photodetectors. *ACS Nano* **2019,** *13* (10), 11988-11995.

19. Carey, T.; Cacovich, S.; Divitini, G.; Ren, J.; Mansouri, A.; Kim, J. M.; Wang, C.; Ducati, C.; Sordan, R.; Torrisi, F., Fully inkjet-printed two-dimensional material

field-effect heterojunctions for wearable and textile electronics. *Nat. Commun* **2017,** *8* (1), 1202.

20. Fowles, J.; Banton, M.; Klapacz, J.; Shen, H., A toxicological review of the ethylene glycol series: Commonalities and differences in toxicity and modes of action. *Toxicol. Lett.* **2017,** *278*, 66-83.

21. Liu, K.; Sakurai, M.; Aono, M., ZnO-based ultraviolet photodetectors. *Sensors (Basel)* **2010,** *10* (9), 8604-8634.

22. Hou, B.; Cho, Y.; Kim, B. S.; Hong, J.; Park, J. B.; Ahn, S. J.; Sohn, J. I.; Cha, S.; Kim, J. M. Highly Monodispersed PbS Quantum Dots for Outstanding Cascaded-Junction Solar Cells. *ACS Energy Lett.* **2016,** *1* (4), 834-839

23. Son, Y.; Kim, C.; Yang, D. H.; Ahn, D. J., Spreading of an Inkjet Droplet on a Solid Surface with a Controlled Contact Angle at Low Weber and Reynolds Numbers. *Langmuir* **2008,** *24* (6), 2900-2907.

24. Fromm, J. E., Numerical Calculation of the Fluid Dynamics of Drop-on-Demand Jets. *IBM J. Res. Dev* **1984,** *28* (3), 322-333.

25. Deegan, R. D.; Bakajin, O.; Dupont, T. F.; Huber, G.; Nagel, S. R.; Witten, T. A., Capillary flow as the cause of ring stains from dried liquid drops. *Nature* **1997,** *389* (6653), 827-829.

26. Centeno, G.; Sánchez-Reyna, G.; Ancheyta, J.; Muñoz, J. A. D.; Cardona, N., Testing various mixing rules for calculation of viscosity of petroleum blends. *Fuel* **2011,** *90* (12), 3561-3570.

27. Nemtsev, I. V.; Shabanova, O. V.; Shestakov, N. P.; Cherepakhin, A. V.; Zyryanov, V. Y., Morphology stability of polymethylmethacrylate nanospheres formed in water–acetone dispersion medium. *Appl. Phys. A* **2019,** *125* (10), 738.

28. Birnie, D. P., A Model for Drying Control Cosolvent Selection for Spin-Coating Uniformity: The Thin Film Limit. *Langmuir* **2013,** *29* (29), 9072-9078.

29. Uchiyama, H.; Matsui, T.; Kozuka, H., Spontaneous Pattern Formation Induced by Bénard–Marangoni Convection for Sol–Gel-Derived Titania Dip-Coating Films: Effect of Co-solvents with a High Surface Tension and Low Volatility. *Langmuir* **2015,** *31* (45), 12497-12504.

30. Majumder, M.; Rendall, C. S.; Eukel, J. A.; Wang, J. Y. L.; Behabtu, N.; Pint, C. L.; Liu, T.-Y.; Orbaek, A. W.; Mirri, F.; Nam, J.; Barron, A. R.; Hauge, R. H.; Schmidt, H. K.; Pasquali, M., Overcoming the "Coffee-Stain" Effect by Compositional Marangoni-Flow-Assisted Drop-Drying. *J. Phys. Chem. B* **2012,** *116* (22), 6536-6542.

31. Zhang, N.; Chao, D. F., Mechanisms of convection instability in thin liquid layers induced by evaporation. *INT COMMUN HEAT MASS* **1999,** *26* (8), 1069-1080.

32. Hossain, R. F.; Deaguero, I. G.; Boland, T.; Kaul, A. B., Biocompatible, large-format, inkjet printed heterostructure MoS2-graphene photodetectors on conformable substrates. *NPJ 2D Mater. Appl.* **2017,** *1* (1), 28.

33. Birnie, D. P., Rational solvent selection strategies to combat striation formation during spin coating of thin films. *J Mater. Res.* **2011,** *16* (4), 1145-1154.

34. Lee, H.; Lee, K.; Park, J. T.; Kim, W. C.; Lee, H., Well-Ordered and High Density Coordination-Type Bonding to Strengthen Contact of Silver Nanowires on Highly Stretchable Polydimethylsiloxane. *Adv. Funct. Mater* **2014,** *24* (21), 3276-3283.

35. Tran, V.-T.; Wei, Y.; Yang, H.; Zhan, Z.; Du, H., All-inkjet-printed flexible ZnO micro photodetector for a wearable UV monitoring device. *Nanotechnology* **2017,** *28* (9), 095204.

36. Shao, D.; Yu, M.; Sun, H.; Hu, T.; lian, J.; Sawyer, S., High responsivity, fast ultraviolet photodetector fabricated from ZnO nanoparticle–graphene core–shell structures. *Nanoscale* **2013,** *5* (9), 3664-3667.

37. Liu, B.; Wang, Z.; Dong, Y.; Zhu, Y.; Gong, Y.; Ran, S.; Liu, Z.; Xu, J.; Xie, Z.; Chen, D.; Shen, G., ZnO-nanoparticle-assembled cloth for flexible photodetectors and recyclable photocatalysts. *J. Mater. Chem* **2012,** *22* (18), 9379-9384.

38. Gong, M.; Liu, Q.; Cook, B.; Kattel, B.; Wang, T.; Chan, W.-L.; Ewing, D.; Casper, M.; Stramel, A.; Wu, J. Z., All-Printable ZnO Quantum Dots/Graphene van der Waals Heterostructures for Ultrasensitive Detection of Ultraviolet Light. *ACS Nano* **2017,** *11* (4), 4114-4123.

39. Pace, G.; Grimoldi, A.; Sampietro, M.; Natali, D.; Caironi, M., Printed photodetectors. *Semicond. Sci. Technol* **2015,** *30* (10), 104006.

40. Carey, T.; Cacovich, S.; Divitini, G.; Ren, J.; Mansouri, A.; Kim, J. M.; Wang, C.; Ducati, C.; Sordan, R.; Torrisi, F. Fully inkjet-printed two-dimensional material field-effect heterojunctions for wearable and textile electronics. *Nat. Commun* **2017,** *8* (1), 1202.

Table of Contents (TOC)